1-1-2008

Ground-based optical and Spitzer infrared imaging observations of comet 21p/Giacobini-Zinner

Jana Pittichová

Charles E. Woodward

Michael S. Kelley
University of Central Florida

William T. Reach

The Astronomical Journal, 136:1127–1136, 2008 September doi:10.1088/0004-6256/136/3/1127

GROUND-BASED OPTICAL AND *SPITZER* INFRARED IMAGING OBSERVATIONS OF COMET 21P/GIACOBINI-ZINNER

Jana Pittichová[1,2], Charles E. Woodward[3], Michael S. Kelley[4], and William T. Reach[5]
[1] Institute for Astronomy, University of Hawaii, 2680 Woodlawn Drive, Honolulu, HI 96822, USA; jana@ifa.hawaii.edu
[2] Astronomical Institute of Slovak Academy of Sciences, Dúbravská cesta 9, Bratislava IV, 84504, Slovakia
[3] Department of Astronomy, School of Physics and Astronomy, 116 Church Street, S. E., University of Minnesota, Minneapolis, MN 55455, USA; chelsea@astro.umn.edu
[4] Department of Physics, University of Central Florida, 4000 Central Florida Blvd., Orlando, FL 32816-2385, USA; msk@physics.ucf.edu
[5] *Spitzer* Science Center, MS 220-6, California Institute of Technology, Pasadena, CA 91125, USA; reach@ipac.caltech.edu
Received 2008 April 17; accepted 2008 June 20; published 2008 August 11

ABSTRACT

We present ground-based optical and *Spitzer Space Telescope* infrared (IR) imaging observations of the ecliptic (Jupiter-family) comet 21P/Giacobini-Zinner, the parent body of the Draconid meteor stream, during its 2005 apparition. The onset of nucleus activity occurred at a pre-perihelion heliocentric distance, $r_h \simeq 3.80$ AU, while post-perihelion 21P was dusty (peak $Af\rho = 131$ cm^{-1}) and active out to heliocentric distances $\gtrsim 3.3$ AU following a logarithmic slope with r_h of -2.04. Coma colors, $V - R = 0.524 \pm 0.003$, $R - I = 0.487 \pm 0.004$, are redder than solar, yet comparable to colors derived for other Jupiter-family comets. A nucleus radius of 1.82 ± 0.05 km is derived from photometry at quiescence. *Spitzer* images post-perihelion exhibit an extensive coma with a prominent dust tail, where excess emission (over the dust continuum) in the 4.5 μm Infrared Array Camera (IRAC) image arises from volatile gaseous CO and/or CO_2. No dust trail was detected (3σ surface brightness upper limit of 0.3 MJy sr^{-1} pixel^{-1}) along the projected velocity vector of comet 21P in the MIPS 24 μm image suggesting that the number density of trail particles is $\lesssim 7 \times 10^{-11}$ m^{-3}. The bolometric albedo of 21P derived from the contemporaneous optical and *Spitzer* observations is $A(\theta = 22^\circ) = 0.11$, slightly lower than values derived for other comets at the same phase angle.

Key words: comets: individual (21P/Giacobini-Zinner) – infrared: solar system – meteors, meteoroids

1. INTRODUCTION

Comet nuclei formed beyond the protoplanetary disk frost line (heliocentric distances, $r_h \gtrsim 5$ AU; Lunine & Gautier 2004) among the giant planets and were scattered into the Kuiper Belt and beyond into the Oort Cloud (OC). Since their formation, the interiors and surfaces of most comets have remained at temperatures below 140 K while in "cold storage" in the Kuiper Belt or the OC (Meech & Svoreň 2004). Moreover, most nucleus surfaces have remained below 400 K even during perihelion passage. At such low temperatures, dust mineralogy remains stable and each comet nucleus retains a record of the minerals, ices, and volatiles extant in the comet agglomeration zones in the early solar system. Furthermore, comet nuclei may retain their primordial compositional inhomogeneities so that different topographic regions would have different compositions (e.g., Dello Russo et al. 2007), leading to variations in volatile production rates as a function of nucleus rotation. Nucleus heterogeneities are apparent in the fly-by imagery of ecliptic comet 9P/Tempel 1. Regions of distinct topography (Belton et al. 2007), and spatially distinct sites of water and CO_2 release (Feaga et al. 2007; A'Hearn et al. 2005) are evident, as well as heterogeneities in surface and subsurface composition (Harker et al. 2007; Kadono et al. 2007).

There are two general dynamical families of comets, classified by derived orbital elements (i.e., Tisserand parameter, T_J) based on current observations. Nearly-isotropic comets (NICs; $T_J < 2$) have orbits that are approximately uniformly distributed in inclination, and are derived from the OC. Ecliptic comets (EC) have orbits that are confined to inclinations near the ecliptic plane, $2 \lesssim T_J \lesssim 3$, and originate in the Kuiper Belt. Resulting from frequent perihelion passage over the 4.0–4.5 Gyr period since their formation, EC comets have become noticeably less active than OC comets, characterized by lower gas and dust-production rates. Multi-epoch spectral energy distributions (SEDs) of ECs, from which comae dust properties can be constrained, are needed to assess the possible interrelationships between their reduced activity levels and dust properties.

The study of the physical properties of both cometary nuclei and comae is equally important to our understanding of the outer solar system environment during the era of icy planetesimal formation, and complements efforts to discern conditions extant in early protoplanetary disks during the epoch of planetesimal formation. We present new optical and contemporaneous *Spitzer* observations of comet 21P/Giacobini-Zinner obtained during its 2005 apparition as part of a larger survey of both ECs and NICs (e.g., Kelley et al. 2006). Ground-based optical observations enabled us to obtain precise optical photometry to assess variations in dust productivity with heliocentric distance and to study the comet's near-nucleus structures, including its jets and coma. *Spitzer* images at mid-infrared (IR) wavelengths enable the study of the spatial distributions of volatiles and dust in the coma, as well as facilitating investigation of comet trail properties. We describe our observations in Section 2, and discuss analysis of our optical and IR observations in Section 3, while our conclusions are summarized in Section 4.

2. OBSERVATIONS AND REDUCTION

Comet 21P/Giacobini-Zinner was discovered by the French astronomer Michel Giacobini in 1900 and rediscovered two apparitions later, in 1913, by the German astronomer Ernst Zinner. 21P, the parent body of the Draconids (also known as the Giacobinids) meteor shower (Beech 1986), is a

Table 1
Observational Summary Log

Observation Date (UT)	Telescope	r (AU)	Δ (AU)	α[a] (deg)	FWHM[b] ($''$)	Filter Exposures	Integration (s)	Sky[c]
				Pre-perihelion				
2004 Jun 21	UH2.2 m	3.80	3.21	13.61	0.80	$R \times 2$	1200	C
2004 Jun 22	UH2.2 m	3.79	3.21	13.76	0.80	$R \times 3$	300	C
				Post-perihelion				
2005 Oct 20	UH2.2 m	1.76	1.74	33.02	0.60	$R \times 11$	30	P
2005 Oct 22	UH2.2 m	1.78	1.74	32.80	0.76	$V \times 2$, $R \times 3$ $I \times 2$	90	P
2005 Dec 02	*Spitzer*	2.14	1.94	28.19	...	MIPS24 $\times$ 14	10	...
2005 Dec 21	UH2.2 m	2.32	1.72	22.56	0.71	$R \times 13$, $I \times 2$	200	P
2005 Dec 22	UH2.2 m	2.32	1.72	22.32	0.65	$V \times 3$, $R \times 18$ $I \times 3$	150	P
2005 Dec 31	*Spitzer*	2.40	1.89	23.61	...	IRAC 4.5 $\times$ 60	30	...
2005 Dec 31	*Spitzer*	2.40	1.89	23.61	...	IRAC 8.0 $\times$ 60	30	...
2006 Mar 05	UH2.2 m	2.91	2.24	16.37	0.84	$R \times 5$, $I \times 1$	500	C
2006 Mar 06	UH2.2 m	2.92	2.25	16.45	0.73	$V \times 1$, $R \times 4$ $I \times 1$	400	P

Notes.
[a] Phase angle (Sun–Comet–Earth) or (Sun–Comet–*Spitzer*).
[b] Seeing measured from stellar point sources.
[c] Sky shows either cirrus (C) or photometric (P) conditions.

Jupiter-family (i.e., EC with a short period) comet with an orbital period of 6.61 years and an aphelion distance just exterior to Jupiter's orbit. In 1933 a spectacular Giacobini meteor storm was visible across Europe. The 1946 apparition of 21P was especially noteworthy as the comet passed only 0.26 AU from Earth in late September with a visible magnitude $\simeq$7. In early October, an unexpected outburst of activity caused the comet to brighten to sixth magnitude. Every alternate apparition of comet 21P presents favorable observing geometries for observers on Earth, with integrated coma visual magnitudes as high as 7. 21P was also the first comet visited by a spacecraft when the International Cometary Explorer (ICE) flew past at a distance of 7800 km on 1985 September 11 (von Rosenvinge et al. 1986).

2.1. Ground-Based Optical

Optical images of comet 21P/Giacobini-Zinner were obtained on the University of Hawai'i (UH) 2.2 m telescope on Mauna Kea, using a Tektronix 2048 $\times$ 2048 CCD camera at the $f/10$ focus of the telescope (image scale of 0.219$''$pixel^{-1}) through a Kron-Cousins filters set (V: λ_o = 5450 Å, $\Delta\lambda$ = 836 Å; R: λ_o = 6460 Å, $\Delta\lambda$ = 1245 Å; I: λ_o = 8260 Å, $\Delta\lambda$ = 1888 Å), during multiple observation runs from 2004 June, 2005 October and December, and 2006 March. The camera read-noise was 6.0 e^- with a gain of 1.74 e^- per ADU. Non-sidereal guiding at the cometary rates of motion, derived from the JPL/Horizons ephemeris, was used during all image observations. Specific observational details, including orbital geometry for 21P, filters, number of exposures, individual exposure times, and sky conditions are summarized in Table 1.

The optical CCD frames were reduced with standard IRAF[6] routines. All the images were reduced using flat field images taken during the evening and morning twilight sky and cleaned of bad pixels and cosmic rays. The frames were calibrated with the standard stars of Landolt (1992), which were observed on each photometric night. Observations of typically 20 standard stars were obtained over a range of air masses, and with a wide dispersion of color to fit for both extinction and color terms. Apparent magnitudes of 20–30 field stars of equal or greater brightness to the comet on each frame were measured in order to do relative photometry. After correcting the measured magnitudes for extinction, we used the deviations of the field star magnitudes in each frame from their nightly average values to correct for frame-to-frame extinction in the comet's measured signal. Figure 1 shows selected individual optical images for each ground-based observing run.

2.2. Spitzer Imaging

We observed comet 21P with the Infrared Array Camera (IRAC; Fazio et al. 2004) and the Multiband Imaging Photometer for *Spitzer* (MIPS; Rieke et al. 2004) on the *Spitzer Space Telescope* (Werner et al. 2004), post-perihelion as summarized in Table 1. The MIPS astronomical observation request (AOR) used the 24 μm array in mapping mode to assess the existence of the comet's dust trail (AOR key 0015734784, 22$'$ $\times$ 15$'$ map). A duplicate MIPS observation was taken 25 h later to observe the sky background after the comet had moved out of the frame (AOR key 0015734528). The IRAC AOR utilized the 4.5 and 8.0 μm arrays to obtain complementary deep photometry of the coma (AOR key 0013820160, 6.7$'$ $\times$ 5.5$'$ map).

The IRAC and MIPS observations were calibrated with *Spitzer* pipelines S13.2.0 and S13.0.1, respectively. The images were mosaicked in the rest frame of the comet with the MOPEX software (Makovoz & Kahn 2005) at the native IRAC and MIPS pixel scales (1.22$''$pixel^{-1} for IRAC, 2.5$''$pixel^{-1} for MIPS 24 μm). The MIPS background observation was mosaicked with the same size, scale, and orientation as the primary observation, and then subtracted from the primary. Before mosaicking, all images were masked to remove cosmic rays and bad pixels. No additional corrections were necessary.

[6] IRAF is distributed by the National Optical Astronomy Observatory, which is operated by the Association of Universities for Research in Astronomy, Inc., under cooperative agreement with the National Science Foundation.

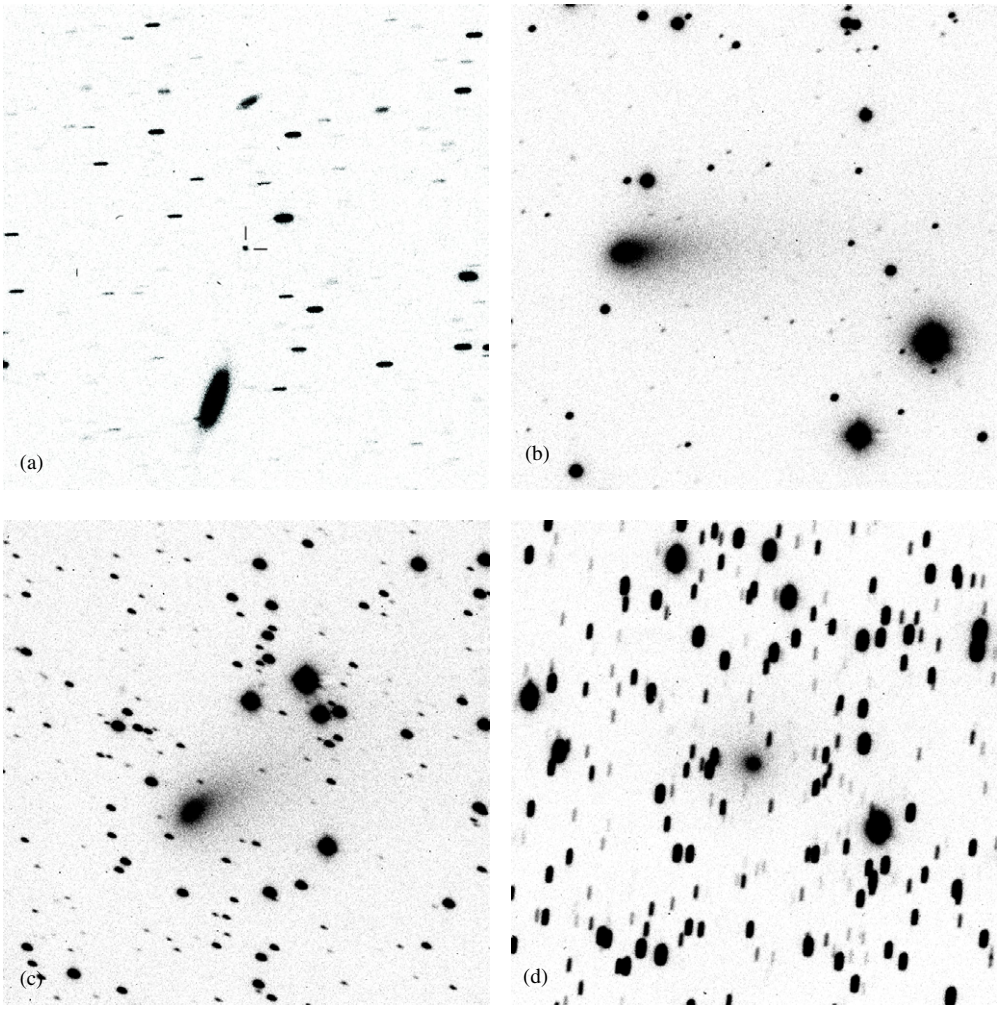

Figure 1. Selected optical images of comet 21P/Giacobini-Zinner obtained on the UH 2.2 m telescope. The fields of view are 180″ × 180″ in size. North is up and east is to the left in all the images, while the stellar point sources appear elongated due to non-sidereal track rates of the telescope. (a) 2004 June 21, $r_h = 3.80$ AU pre-perihelion, the comet is marked by the ticks in the image; (b) 2005 October 22, $r_h = 1.76$ AU post-perihelion; (c) 2005 December 21, $r_h = 2.32$ AU post-perihelion; and (d) 2006 March 05, $r_h = 2.91$ AU post-perihelion.

Our IRAC image of comet 21P was obtained at a post-perihelion distance of $r_h = 2.40$ AU. Analysis of the secular optical light curves of 21P by Ferrín (2005) suggests that the nucleus turn-on time (marking the onset of steady coma activity) occurs pre-perihelion near 3.7 AU, whereas the onset of nucleus turn-off may not occur until 21P reaches 5.4 AU. Indeed Tancredi et al. (2000) argue that 21P is active at 4.5 AU. The IRAC 4.5 μm image, Figure 2, shows an extended coma surrounding the nucleus. Discussion of this extended emission is presented in Section 3.7. The *Spitzer* MIPS 24 μm image is presented in Figure 3.

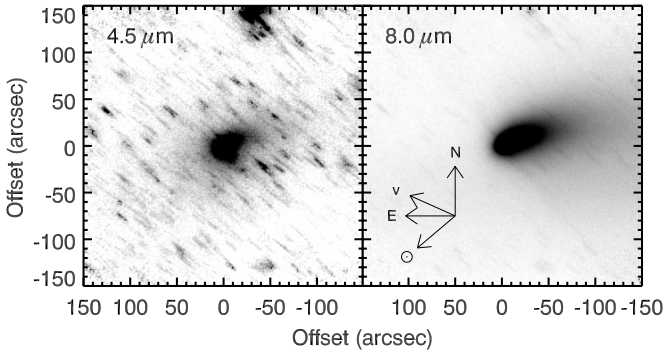

Figure 2. Comet 21P/Giacobini-Zinner *Spitzer* IRAC images obtained at $r_h = 2.40$ AU post-perihelion. The gray scales range from 0.05 to 0.11 MJy sr^{-1} for the 4.5 μm image, and 1.79 to 3.11 MJy sr^{-1} for the 8.0 μm image. The arrows mark north, east, the projected sun angle ($\odot$), and the projected velocity of the comet (v).

3. DISCUSSION

3.1. Optical Photometry

The photometry derived from our optical images enable investigation of cometary activity with heliocentric distance, estimation of dust-production rates ($Af\rho$; A'Hearn et al. 1984), determination of the coma color, and construction of rotational light curves.

The stellar and comet fluxes were extracted from the optical CCD frames using the IRAF photometry routine "PHOT" with a circular aperture. This routine automatically finds the centroid of the image within the user-specified photometry aperture, with the sky background determined in an annulus lying immediately outside the photometry aperture (for stellar images), or selected from an average of many sky positions outside the extent of any coma. Photometric apertures between 1″ and 5″ were used

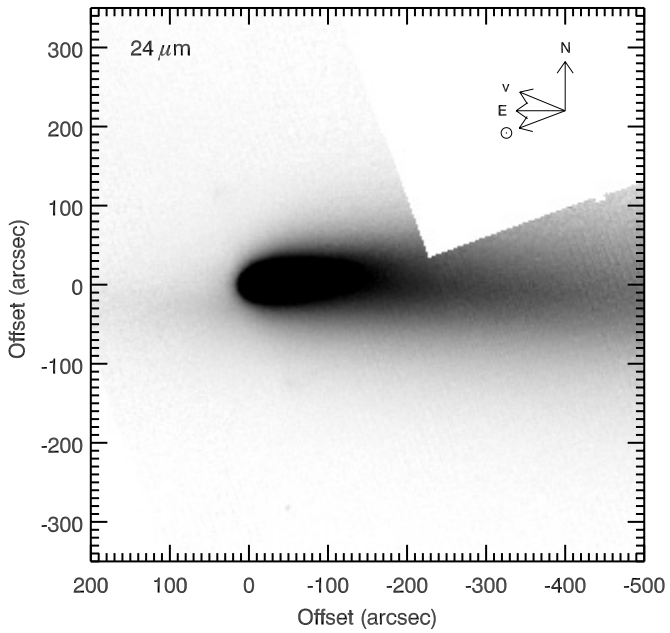

Figure 3. Comet 21P/Giacobini-Zinner *Spitzer* MIPS 24 μm image obtained at $r_h = 2.14$ AU post-perihelion. The gray scale ranges from 0.21 to 6.80 MJy sr^{-1}. The arrows mark north, east, the projected sun angle ($\odot$), and the projected velocity of the comet (v).

for the comet photometry with the average sky background determined using sky annuli with an inner radii of 8.0″–10″, with widths of 4.0″–5.0″. Averaging many sky background positions adjacent to the comet also enabled rejection of any bad pixels or field stars found in individual sky annuli circumscribing the aperture used to determine the comet surface brightness. The smallest possible aperture that minimized contamination from extended surface brightness of the coma while including most of the flux from the nucleus (with respect to the full width at half-maximum seeing determined from stellar point sources on the frame) was 3″. A 4″ aperture was also used for the field stars used for differential photometry. After correcting the measured magnitudes for extinction, we used the deviations of the field stars from their nightly average magnitudes in each frame to correct for frame-to-frame extinction variations in the comet's measured signal.

For the non-photometric data (Table 1) from the nights of 2004 June 21 and 22, and 2006 March 5, the comet fields were re-imaged under photometric conditions on 2005 May 18 and 2006 June 03 for "boot-strap" calibration. Multiple ($\gtrsim$20) field stars were measured on both the calibration images and the non-photometric images and differential photometry was used to compute the photometrically-calibrated brightness of the comet. This technique works well for up to $\simeq$0.5 mag of extinction.

3.2. Heliocentric Activity

The most direct indicator of nucleus activity is the appearance of visible coma around a comet nucleus. Our first observations of 21P (Figure 1(a)) were obtained on 2004 June (−375 days before perihelion) when the comet was at a large heliocentric distance, $r_h = 3.80$ AU. No coma was evident on individual images, nor on the composite image created by mosaicking the 2–3 images obtained on each night to increase the signal-to-noise ratio of any diffuse coma emission. Absence of a detectable coma −375 days before perihelion is consistent with 1991 apparition observations of Mueller (1992) who found no coma at −367 days before perihelion, yet a clearly detectable coma at −334 days. Our observations indicate that the heliocentric turn-on point for 21P nucleus activity this apparition was similar to the behavior observed in the 1991.

The average R-band magnitude measured for 21P on a given night is summarized in Table 2, column 3, as is the reduced magnitude, column 6. The reduced magnitude, $m(1, 1, 0)$, i.e., the observed magnitude normalized to unit heliocentric distance, r_h, and geocentric distance, Δ, for zero phase angle, α, was derived from the relationship for active comets

$$m(1, 1, 0) = m_R - 2.5\,n\,\log(r_h) - 2.5\,k\,\log(\Delta) - \alpha\beta, \quad (1)$$

where m_R is the R-band photometric magnitude measured in a 3″ circular aperture, β is the linear phase coefficient =0.035 mag deg^{-1}, and n and k are constants, taken to be unity and 2 respectively. Nominally, values for these two latter constants (n being dependent on dust grain production, coma shape, and size) are derived from modeling a given comet at a variety of heliocentric distances if there are sufficient observational data. Equation (1) is also appropriate for expressing the brightness of an active comet with a spherical coma around the nucleus (measured in a circular aperture, as described by Meech & Svoreň 2004), as opposed to the relation used by Ferrín (2005) which is the proscription for the brightness of bare nuclei (non-active stage). Computation of the reduced magnitude is a standard method that enables of photometric data of an individual comet obtained at a variety of heliocentric distances (different activity level) to be intercompared. For 21P, we obtained observations of the comet when there was no visible coma, when the comet exhibited a small coma around the nucleus, and when the comet was highly active displaying a significant, spatially extended coma with an elongated tail. To properly intercompare variations in the integrated aperture surface brightness, the R-band photometric magnitudes were determined by measuring the comet's brightness in a small 3″ circular aperture centered on the nucleus. Use of this small nucleo-centric aperture minimized the coma contribution to the measured flux density, and allowed estimation of the nucleus brightness consistent with the uniform azimuthally-averaged surface brightness profile.

Our observations of 21P span a range of heliocentric distance, both pre- and post-perihelion (Table 1), thus we can examine trends in $m(1, 1, 0)$ with r_h. Figure 4 shows the variation in the reduced magnitude as a function of r_h derived from R-band photometry, where the dotted horizontal lines represent the likely brightness range for a bare nucleus, calculated from our photometry data when no coma was seen. Evidently, cometary activity commenced near $r_h \simeq 3.80$ AU this apparition of 21P, and the majority of our optical observations and all of our *Spitzer* images were obtained while the comet was in an active state.

3.3. Coma Colors

Average coma color differences ($V - R$, $R - I$) are also listed in Table 2 for dates when multi-wavelength observations were conducted. The average colors of comet 21P, $V - R = 0.524 \pm 0.003$, $R - I = 0.487 \pm 0.004$ are redder than the respective solar colors, 0.36 and 0.28, in the Krons-Cousins system, transforming the Johnson solar colors (Allen 1973) using the relation of Fernie (1983). Band emission from gaseous molecular species, such as C_2 ($\lambda \approx$ 5520 Å), NH_2 ($\lambda \approx$ 6335 Å), and CN ($\lambda \approx$ 9180 Å), or atomic O I ($\lambda = 6300$ Å ^{1}D) potentially could contribute significantly

Table 2
Derived Optical Photometric Parameters

Observation Date (UT)	r_h (AU)	R-band[a] (mag)	$V-R$[a] (mag)	$R-I$[a] (mag)	$m(1,1,0)$ (mag)	$Af\rho$ (cm)
			Pre-perihelion			
2004 Jun 21	3.80	21.89 ± 0.04	...	...	17.19	4.80
2004 Jun 22	3.79	21.95 ± 0.06	...	...	17.24	4.55
			Post-perihelion			
2005 Oct 20	1.76	15.91 ± 0.01	...	...	12.82	130.66
2005 Oct 22	1.78	16.05 ± 0.01	0.53 ± 0.01	0.49 ± 0.01	12.89	124.47
2005 Dec 21	2.32	17.05 ± 0.01	...	0.49 ± 0.01	13.74	83.00
2005 Dec 22	2.32	17.07 ± 0.01	0.52 ± 0.01	0.48 ± 0.01	13.76	82.07
2006 Mar 05	2.91	16.37 ± 0.01	...	0.48 ± 0.01	14.80	39.06
2006 Mar 06	2.92	18.48 ± 0.01	...	...	14.61	46.50

Note. [a] Average color measured in a 3″ circular aperture.

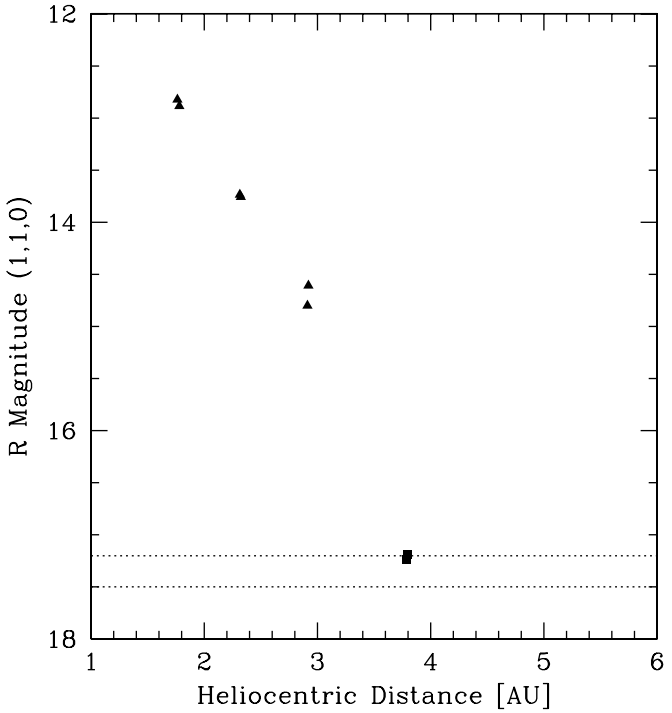

Figure 4. Comet 21P/Giacobini-Zinner broadband data reduced to unit heliocentric distance, r_h (AU), geocentric distance, Δ (AU), and zero phase plotted versus r_h. The square symbols are for pre-perihelion data and the triangular symbols are for post-perihelion data. The dotted horizontal lines represent the likely brightness range for a bare nucleus, calculated from our photometry data when no coma was seen (see Table 2).

to the flux density of comet comae observed within our *VRI* broadband filters. However, optical spectra of Fink & Hicks (1996) indicates that band and line emission from these species is relatively weak in the coma of 21P.

21P also lies along the $(R-I)$ versus $(V-R)$ color–color trend line of Jupiter-family comet nuclei attributed by Snodgrass et al. (2005) to albedo variation (in Section 3.5 we derive an dust albedo estimate for 21P), although we cannot quote a precise value for the nucleus color of 21P due to coma contamination. Broadband colors of cometary nuclei are related to surface properties of the nucleus (Davidsson & Skorov 2002) and provide a metric to compare cometary nuclei to other small solar system bodies and to assess which parent body populations give rise to Jupiter-family comets. The bluer color of 21P and other Jupiter-family comets, as compared to the mean color of Kuiper-Belt Object/Trans-Neptunian Object populations, $V-R = 0.60 \pm 0.07$ (Snodgrass et al. 2005), suggests that cometary activity and surface processing in the inner solar system have altered the primitive surfaces of these nuclei agglomerated from materials in the Kuiper Belt (e.g., Jewitt 2002; Wooden et al. 2004).

3.4. Dust-Production Rates

The quantity $Af\rho$ of a comet, a proxy describing the dust-production rate (A'Hearn et al. 1984), is often used to describe nucleus activity vigor, and to distinguish between dusty and inactive comet taxonomies. $Af\rho$ is given by

$$Af\rho = (2.467 \times 10^{19}) \frac{r_h^2 \Delta}{a} \frac{F_{\rm obs}}{F_\odot}, \quad (2)$$

where A is the wavelength-dependent albedo of dust particles, f is the filling factor of grains (total cross-section), ρ is the linear radius of the aperture at the comet, r_h and Δ are heliocentric and geocentric distances (AU), a is the angular diameter of the field of view (in arcseconds), $F_{\rm obs}$ is the observed cometary flux and $F_\odot$ is the solar flux. The $Af\rho$ parameter is typically expressed in centimeters. By providing a metric to quantify a comet's level of dust output (large $Af\rho$ values indicate higher activity), one can ascertain the dust contribution to a set of photometric measurements and assess the heliocentric dependence of dust-production rates in a given comet.

R-band values of $Af\rho$ for 21P derived from our photometry are summarized in column 7 of Table 2 and are plotted as a function of r_h in Figure 5. Peak dust-production rates of 131 cm^{-1} occurred just post-perihelion. We fit the post-perihelion $Af\rho$ values with a function of the form Cr_h^k using the least absolute deviation method (Press et al. 1992). Our best-fit values are $C = 414.4$ cm, $k = -2.04$. The pre-perihelion observations do not span a large enough range of r_h to derive a slope. Our post-perihelion $Af\rho$ slope ($1.76 \lesssim r_h(\mathrm{AU}) \lesssim 2.92$) is comparable to the pre-perihelion value of -2.08 ± 0.15 derived by A'Hearn et al. (1995) based on observations obtained when 21P was at $r_h \simeq 1.34$ AU. However, A'Hearn et al. (1995) find a significantly larger value ($k = +0.38 \pm 0.16$) when the 21P is interior to 1.86 AU post-perihelion suggesting that the comet's activity peaks just after perihelion passage.

3.5. IR Photometry, Optical to IR SED, and the Dust Albedo

We measured the flux of comet 21P in the MIPS and IRAC images using the aper.pro procedure of the IDL Astronomy

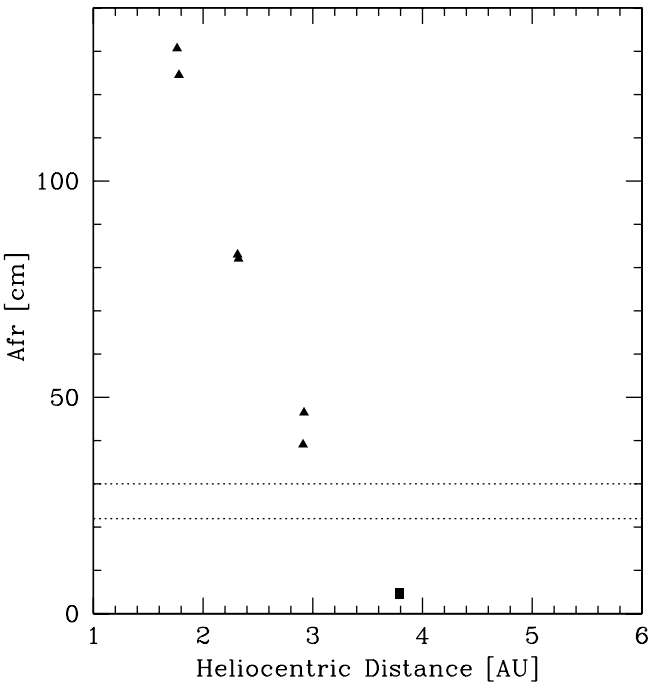

Figure 5. $Af\rho$ values for comet 21P/Giacobini-Zinner as a function of heliocentric distance, r_h (AU), for the period between 2004 June through 2006 March. The square symbols are for pre-perihelion data and the triangular symbols denote post-perihelion data.

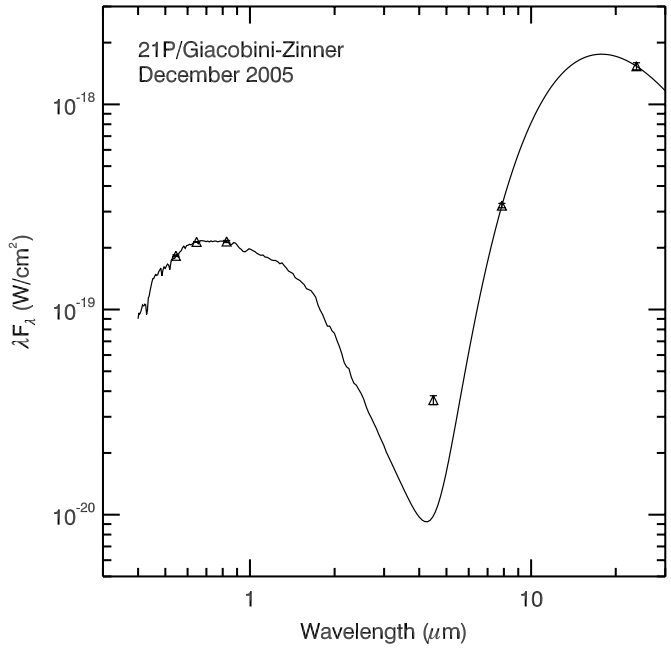

Figure 6. The SED derived for comet 21P/Giacobini-Zinner from ground-based optical and *Spitzer* photometry obtained in 2005 December. The smooth curve is the best-fit curve consisting of a scaled, reddened solar spectrum to represent the scattered light at the optical wavelengths, plus a scaled Planck function, to represent the thermal emission from the IR wavelengths.

User's Library (Landsman 1993). The 2005 December IRAC, MIPS, and optical photometry are all measured at different heliocentric distances ($r_h = 2.1 - 2.4$ AU), observing geometries ($\Delta = 1.7 - 1.9$ AU), and spatial resolutions. However, differences in observational circumstances are small such that simple scaling laws can be applied to the photometry to create a composite 0.5–24 μm SED of comet 21P. For reasons discussed below, we elect to correct the IR photometry (Section 2.2) to match the observing conditions of the optical measurements (Section 2.1).

First, we correct the IR photometry for the limited resolution of the *Spitzer* telescope, as compared to the optical data. The IRAC and MIPS images are diffraction limited and stellar sources have full width at half-maximum $\approx$ 1.4″, 2.0″, and 6″ at 4.5, 8.0, and 24 μm (Fazio et al. 2004; Rieke et al. 2004). The 24 μm point-spread function (PSF) is too broad to compare to the 3″ R-band photometry in Table 2 (column 3), and the IRAC PSF is marginally appropriate. To derive the IR photometry in an aperture size of 3741 km (corresponding to the optical photometry, 3″ at 1.72 AU), we measure the comet's IR coma with increasingly larger apertures and use a curve-of-growth analysis to estimate the fluxes at apertures comparable to or smaller than the resolution of the *Spitzer* instruments. We examined the logarithmic profile of the optical data to verify that the coma slope at moderate sized apertures ($\rho \approx 10''$) extends into the inner coma ($\rho \approx 3''$). The photometry at 10″ and the coma logarithmic slopes are presented in Table 3.

Next we correct the IRAC and MIPS photometry for the differences in observer–comet distance. The correction is simply $(\Delta_{\rm opt}/\Delta_{\rm IR})^2$: 0.93 for IRAC, and 1.18 for MIPS.

Finally, we scale the IRAC and MIPS photometry to match the heliocentric distance ($r_h = 2.32$ AU) of the optical observations. There are two effects that depend on r_h: the temperature of the dust, and the dust production of the comet. To correct for changes in the dust production, we scale the photometry using the $Af\rho$ heliocentric distance trend derived for 21P, $r_h^{-2.04}$ (Section 3.4). The MIPS photometry is scaled by a factor of 0.86 and the IRAC photometry scaled by 1.08. To correct for the dust temperature, we scale the photometry by $B_\lambda(T_{\rm opt})/B_\lambda(T_{\rm IR})$, where B_λ is the Planck function, and $T_{\rm opt}$ and $T_{\rm IR}$ are the dust temperatures at the optical and IR heliocentric distances, which we set to the blackbody temperature, $T = 278\, r_h^{-0.5}$ K. The scale factors are 1.37 for $\lambda = 4.5$ μm, 1.20 for $\lambda = 8.0$ μm, and 0.88 for $\lambda = 23.7$ μm for the IRAC and MIPS data, respectively.

Our measured fluxes, azimuthally averaged surface brightness profile logarithmic slopes, and the corrected photometry are presented in Table 3. The total SED of the comet is presented in Figure 6. The optical magnitudes of Table 2 were converted to flux units using the zero magnitude flux densities of 3600 Jy (V-band), 3090 Jy (R-band), and 2550 Jy (I-band). We fit the SED with a scaled, reddened solar spectrum to represent the scattered light at the optical wavelengths, plus a scaled Planck function, to represent the thermal emission from the IR wavelengths. We exclude the gas contaminated 4.5 μm data point (Section 3.7) from the fit. Solar spectrum reddening (the spectral slope) is typically expressed as percent per 0.1 μm (e.g., Jewitt & Meech 1986). A negative spectral slope represents a bluing of the spectrum. Our observations constrain the scattered light reddening between the V- and R-bands, and the R- and I-bands. Following Jewitt & Meech (1986), we express the reddening with the linear slope $S'(\lambda_1, \lambda_2)$ expressed as % per 0.1 μm. At optical wavelengths, our computed slopes for comet 21P (see Table 2) are $S'(V, R) = (15 \pm 1)$% per 0.1 μm, and $S'(R, I) = (11 \pm 1)$% per 0.1 μm. The former slope of the reflectivity gradient is in good agreement with the average value of $S'(B, R) = (13 \pm 5)$% per 0.1 μm derived by Jewitt & Meech (1986) for comets, while the latter $S'(R, I)$ slope value agrees with the general trend of bluer scattering at longer wavelengths (see Figure 4 of Jewitt & Meech 1986). Indeed, Jewitt & Meech (1986) observed 21P in the near-IR and found $S'(J, H) = 3.5$%

Table 3
Derived Mid-Infrared Photometric Parameters of 21P

Instrument/ Wavelength (μm)	r_h (AU)	F_λ[a] ($\times 10^{-20}$ W cm^{-2} μm^{-1})	S.B. Slope, k[b]	F_λ[c] ($\times 10^{-20}$ W cm^{-2} μm^{-1})
IRAC 4.5	2.40	1.63 ± 0.05	-1.10 ± 0.07	0.81 ± 0.04
IRAC 8.0	2.40	9.54 ± 0.20	-1.01 ± 0.06	4.08 ± 0.10
MIPS 24.0	2.14	20.6 ± 0.8	-0.99 ± 0.03	6.47 ± 0.26

Notes.
[a] F_λ measured in a 10″ radius (ρ) aperture.
[b] The logarithmic slope of the azimuthally averaged, surface brightness profile.
[c] F_λ equivalent to a 3741 km radius aperture with the same observing circumstances as the 2005 December 22 UT optical observations (i.e., corrected for *Spitzer*–comet distances, dust temperature, and activity rate ($Af\rho$).

per 0.1 μm and $S'(H, K) = 0.3\%$ per 0.1 μm. The fit has no degrees of freedom, so we do not present errors or a χ^2 analysis. The best-fit dust temperature is 206 K (∼15% warmer than a blackbody). We derive a bolometric albedo for the dust of comet 21P using Equations (6) and (7) from Gehrz & Ney (1992). The bolometric albedo of 21P is $A(\theta = 22^\circ) = 0.11$, slightly lower than values derived for other comets at the same phase angle ($A(\theta = 22^\circ) \approx 0.16$, Kolokolova et al. 2005), but not unusual.

3.6. Nucleus Size and Light Curves

The size of the equivalent spherical nucleus, R_N, can be estimated from the apparent mean magnitude of comet 21P measured at heliocentric distances when the comet is relatively inactive. Pre-perihelion, $m_R = 21.89 \pm 0.04$ (Table 2), and R_N can be derived from the standard relation

$$A_R R_N^2 = (2.238 \times 10^{22})\, r_h^2\, \Delta^2\, 10^{0.4[m_\odot - m_R + \beta\alpha]}, \qquad (3)$$

where A_R is the geometric albedo, r_h (AU) is the heliocentric distance, Δ (AU) is the geocentric distance, $m_\odot = -27.09$ is the R-band magnitude of the Sun (Russel 1916), β (mag deg^{-1}) is the linear phase coefficient, and α is the phase angle. For 21P, we adopt a value of $A_R = 0.04$ (Lamy et al. 2005; Fernández et al. 2001) and $\beta = 0.035$ mag deg^{-1} which is generally used for most comets with unknown β; however, Ferrín (2005) argue that a $\beta_{\rm mean} = 0.046 \pm 0.013$ may be more appropriate based on the observed phase coefficient for ten comets. We find $r_N = 1.82 \pm 0.05$ km, commensurate with other estimates of nucleus size ranging from 1.0 km derived by Tancredi et al. (2000) or ∼2.1 km value derived from the snapshot survey of Mueller (1992), assuming $A_R = 0.04$.

In principle, variations in the photometric brightness derived from the R-band individual images obtained over ≈2–3 h intervals during the period of 2005 December 21 through 22 (Table 2) can be used to generate a composite light curve yielding estimates of nucleus rotational periods. However, our composite light curve of 21P at this epoch, $r_h = 2.32$ AU exhibits little periodic variation and we are unable to determine a rotational period. 21P was also very active during this epoch, with a significant coma contribution which could mask subtle variations (±0.01 mag) in nucleus flux. A rotational period of 9.5 ± 0.2 h for 21P has been reported by Leibowitz & Brosch (1986).

3.7. Volatiles CO+CO$_2$

Volatiles are frozen as ices or trapped as gases in amorphous water ice in the nuclei of comets (Capria 2002; Prialnik 2002). Cometary activity occurs when gases are released through sublimation or through the exoergic crystallization of amorphous water ice. Water sublimation primarily drives vigorous activity at $r_h \lesssim 5$ AU (Meech & Svoreň 2004), but other volatiles can still be important drivers. At 1.5 AU, Feaga et al. (2007) found that CO_2 gas was correlated with comet 9P/Tempel's southern hemisphere—the location of the strongest dust jet (Farnham et al. 2007)—yet water vapor was more strongly associated with the northern hemisphere.

Some molecular species (e.g., CO) are released not only from the nucleus (native source), but also from within the coma ("distributed" or "extended" source). In the extensively studied, bright OC comet C/1995 O1 (Hale-Bopp), there was evidence for distributed CO sources, possibly arising from icy grains in the coma (Gunnarsson et al. 2003) at large r_h, whereas at $r_h \leqslant 1.5$ AU the strong distributed sources probably arise from the desorption of an organic grain component (Crovisier 1999). Although icy grains may be the distributed source of the CO (Gunnarsson 2003; Bockelée-Morvan et al. 2002), pure-CO ice grains do not survive transport into the coma because of their low sublimation temperatures, 20–100 K (Prialnik et al. 2004).

The IRAC 4.5 μm bandpass encompasses the $CO_2\,\nu_3$-band and the CO 1–0 fundamental band at 4.26 and 4.67 μm, respectively. The CO and CO_2 bands are observed as the dominate components at 3–4 μm in excess of the dust continuum emission in *ISO* spectra of comets Hale-Bopp and 103P/Hartley (Crovisier et al. 1999a, 1999b) and in the ambient coma of 9P/Tempel (Feaga et al. 2007). After removing the dust continuum, the IRAC images can be used to map the CO and CO_2 spatial distributions in the comet coma. In principle, the emission from the two molecules can be decoupled when we consider that CO and CO_2 have different lifetimes in the coma and therefore produce different radial distributions. With a measured radial distribution, we can also test for evidence of an extended source of CO or CO_2. Emission from other prominent volatiles, such as water (Woodward et al. 2007), lie outside the bandpass of the IRAC 4.5 μm filter.

The slope of the CO + CO_2 emission in the *Spitzer* images at 4–16 pixels (corresponding to projected cometocentric distances of 6.6×10^3 km to 2.6×10^4 km) can be determined by subtracting a scaled IRAC 8.0 μm image from the IRAC 4.5 μm image (Figure 2). The IRAC 8.0 μm image is dominated by thermal emission from dust, whereas the 4.5 μm image is a combination of emission from gas, dust thermal emission, and sunlight scattered by dust. The color of sunlight scattered by comet dust varies with wavelength (Jewitt & Meech 1986; Kolokolova et al. 2005), and we cannot constrain the spectral

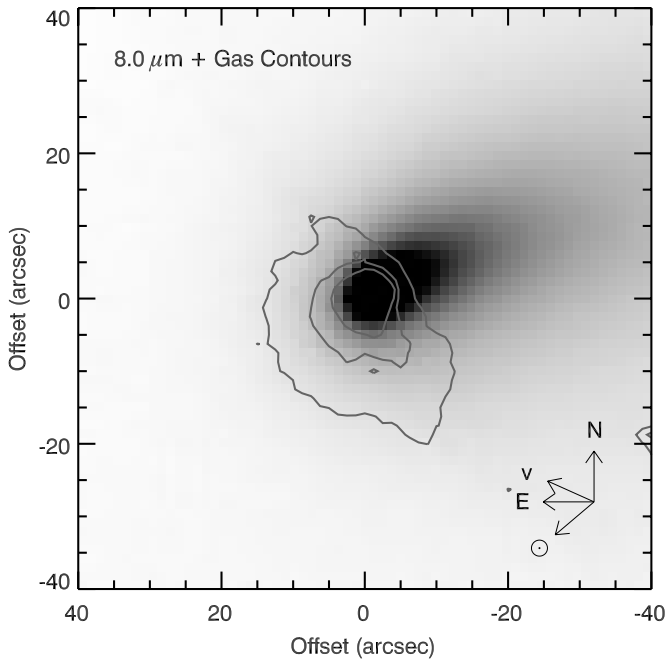

Figure 7. Comet 21P/Giacobini-Zinner *Spitzer* IRAC 8.0 μm image with contours of the excess emission (CO/CO_2 gas) found in the 4.5 μm image. The contours are set to 0.05, 0.10, and 0.15 MJy sr^{-1} and the gray-scale range is 1.79–7.08 MJy sr^{-1}. The surface brightness of the dust tail peaks near the anti-sun angle, and the surface brightness of the gas peaks along the sun angle. The arrows mark north, east, the projected sun angle ($\odot$), and the projected velocity of the comet (v).

slope of the scattered light at 4.5 μm with our data. Rather than estimating the 4.5 μm dust flux from our best-fit SED (Section 3.5), we subtract a scaled 8.0 μm image from the 4.5 μm image to yield an image of the gas emission (Figure 7). Our best scale factor is 0.025 ± 0.003, which we derived from the ratio of the 4.5 μm and 8.0 μm images. We measured the ratio along a 3-pixel wide rectangle positioned on the dust tail from 5 to 40 pixels from the nucleus. The error in the scale factor is the standard deviation of the pixels in the rectangle. We fit the residual surface brightness profile (emission from the gas) in 24° azimuthal steps. The mean surface brightness logarithmic slope is -1.00 (median $= -1.04$, error in the mean $= 0.04$). The derived gas profile is consistent with a long-lived species ejected in a constant outflow from the nucleus, i.e, it shows no evidence for an extended source.

The lifetimes of CO and CO_2 at 2.4 AU are CO $=$ 89 days and $CO_2 = 34$ days (Huebner et al. 1992). For an outflow velocity of 1.0 km s^{-1}, the characteristic length scales are 7.7×10^6 km (CO) and 2.9×10^6 km (CO_2). In our dust subtracted image, there appears to be emission out to 60 pixels from the nucleus ($\simeq 1.0 \times 10^5$ km), but background stars make it difficult to measure the logarithmic slope beyond 20 pixels. Both species are long lived on scale lengths $\leqslant$16 pixels even if the outflow velocity is 0.1 km s^{-1}. From our analysis, both CO and CO_2 are equally viable candidates for the 4.5 μm excess in the difference image, Figure 7. For comparison, in comet Hale-Bopp (Crovisier et al. 1999a), CO_2 was the dominant emission species at 2.9 AU (comet 21P was observed at 2.4 AU).

We can measure the intensity of the gaseous emission and derive upper limits to the CO_2 and CO contributions. We have attempted to remove the dust from the 4.5 μm image; however, emission from the nucleus has not been removed. Although we derived an effective radius from our optical observations (Section 3.6), the orientation, shape, and temperature distribution of the nucleus is unknown at the epoch of the IRAC images. Rather than measuring the flux inside a circular aperture centered on the nucleus, we avoid contamination from the nucleus by measuring the gas coma inside an annulus with an inner radius of 6 pixels, and an outer radius of 8 pixels. We convert the measured annular flux density, $(1.807 \pm 0.027) \times 10^{27}$ erg s^{-1} cm^{-2} Hz^{-1}, into line emission fluxes following the IRAC prescriptions discussed by the *Spitzer* Science Center (2006), where we perform a linear interpolation of values given in the IRAC spectral response tables[7] near the wavelength position of our lines, assuming the residual emission within the effective bandpass of the IRAC 4.5 μm filter is either entirely from either CO_2 ($\lambda = 4.26$ μm) or CO ($\lambda = 4.67$ μm). We find $F_{CO_2} = (3.10 \pm 0.22) \times 10^{-14}$ erg s^{-1} cm^{-2}, and $F_{CO} = (2.86 \pm 0.20) \times 10^{-14}$ erg s^{-1} cm^2. The errors include the IRAC absolute calibration uncertainty of 3%, and a dust subtraction uncertainty of 11%.

The gaseous coma has an azimuthally average profile surface brightness slope of ρ^{-1} (see Table 3); thus we can convert the flux at 6–8 pixels to a flux inside a circular aperture of projected radius 7 pixels, $F_{tot} = 2\pi\rho^2 F_{ann}/A$, where $\rho = 7$ pixels, F_{ann} is the flux measured in the annulus, and A is the area of the annulus in square pixels (e.g., Jewitt & Danielson 1984). The total emission inside this 7 pixel aperture yields an average column density, $\langle N \rangle$, in cm^{-2}, assuming optically thin emission from the expression

$$\langle N \rangle = F_{tot}\, 4\pi\Delta^2 \frac{\lambda}{hc} \frac{r_h^2}{g_{band}} \frac{1}{\pi\rho^2}, \quad (4)$$

where Δ is the observer–comet distance in cm, $\lambda(\mu m)$ is the wavelength of the emission, h is Planck's constant (erg s), c is the speed of light (μm s^{-1}), r_h is the heliocentric distance in AU, g_{band} is the solar fluorescence g-factor at 1 AU in units of s^{-1}, and ρ is the projected radius of the aperture, here in units of cm. We have adopted g-factors given by Crovisier & Encrenaz (1983) of 2.86×10^{-3} s^{-1} for the CO_2 ν_3 band, and 2.46×10^{-4} s^{-1} for the CO 1–0 band, noting that other cited literature values for these g-factors differ by $\lesssim$10%. From Equation (4), we derive average column densities of $(3.13 \pm 0.22) \times 10^{11}$ cm^{-2}, if the emission is solely from CO_2 and $(3.67 \pm 0.27) \times 10^{12}$ cm^{-2}, if the emission is solely from CO.

Bockelée-Morvan et al. (1990) measured OH radio emission profiles in spectra of several comets as a function of r_h, including comet 21P, to derive the expansion velocity of that species. For most low production rate comets ($8.0 \times 10^{28} \leqslant Q_{OH}$(molecules s^{-1}) $\leqslant 1.8 \times 10^{29}$) the expansion velocities are constant for $r_h \gtrsim 1.4$ AU. Radio measurements of the OH production rates of 21P during the 1985 apparition indicate that $Q_{OH} \approx 3.1 \times 10^{28}$ molecules s^{-1}, with little change in the derived expansion velocity, $v_p = 0.70 \pm 0.09$ km s^{-1} (see Table 4, in Bockelée-Morvan et al. 1990) over a range of r_h. Given the lack of a strong r_h dependence of v_p at a distance greater than 1.4 AU, we will adopt 0.70 ± 0.09 km s^{-1} for the parent expansion velocity to estimate the expansion velocities of CO_2 and CO for 21P at 2.4 AU from the Sun. With this velocity, we can derive the production rates, Q, in molecules s^{-1}, for each species:

$$Q = \langle N \rangle 2\rho v \times 10^{10}, \quad (5)$$

where ρ is measured in km, and v in km s^{-1}. The production rates are $Q_{CO_2} \leqslant (5.13 \pm 0.75) \times 10^{25}$ molecules s^{-1}, and

[7] http://ssc.caltech.edu/irac/spectral response.html.

$Q_{CO} \leqslant (6.01 \pm 0.89) \times 10^{26}$ molecules s^{-1}. We note that these are upper limits to the production rates for each species as we cannot distinguish between the two.

Mumma et al. (2000) detected CO at 4.67 μm in the coma of comet 21P at $r_h = 1.2$ AU (pre-perihelion) in 1998 October—the first IR detection of this volatile in a Jupiter-family comet. However, 2 weeks later Weaver et al. (1999) did not detect CO at the same wavelengths. Mumma et al. (2000) suggest that comet 21P has a chemically heterogeneous nucleus, and that the CO was limited to a vent that was not illuminated during the observations conducted by Weaver et al. (1999). This explanation seems reasonable as the comet was near perihelion when seasonal variations of insolation are the greatest. Our IRAC images of comet 21P were obtained at a post-perihelion distance of $r_h = 2.4$ AU. If the vent responsible for the decrease in CO production remains inactive out to 2.4 AU, CO_2 would remain the favored molecule responsible for the IRAC 4.5 μm excess.

3.8. Dust Trails

Determining the cometary dust fraction of the zodiacal dust complex is becoming increasingly important. Recent *Spitzer* discoveries of dust surrounding white dwarfs (Becklin et al. 2005) suggest that mass-loss from cometary bodies (in Kuiper Belt or Oort Cloud analogs) or tidal disruption of asteroidal objects are feeding their circumstellar dust complexes (Su et al. 2007; Reach et al. 2005). Comets lose a large fraction of their mass in dust grains $\gtrsim 100$ μm (Kelley et al. 2008; Reach et al. 2007; Ishiguro et al. 2007; Sykes & Walker 1992). These grains weakly respond to solar radiation pressure and form distinct dynamical structures known as dust trails (Sykes et al. 1988). Trails typically appear to follow their parent nucleus along the comet's projected orbit, although the "trail" may also lead the comet. Dust trails are ubiquitous in Jupiter-family comets, but remain unobserved in OC comets. The existence of OC dust trails is inferred from meteor stream studies of Halley-type comets, which are derived from the OC. For example, the Halley-type comet 55P/Tempel-Tuttle is the parent body of the Leonid meteor stream and at least 80% of JFCs have dust trails (Reach et al. 2007).

The existence of dust trails in comets with perihelia near 1–2 AU has interesting astrobiological significance. Reach et al. (2007) demonstrate that comets have trail mass production rates that are (1) similar to water mass production rates, and (2) greater than the small grain (radii $\lesssim 10$ μm) mass production rates. If the composition of the comet's coma approximates the comet interior, then comet nuclei are mostly refractory in nature (dust-to-ice mass ratio > 1.0), which limits the amount of water a comet could deliver to the surface of a young terrestrial planet. Comet 21P is the parent body of the Draconid meteor stream (Beech 1986), which can produce exceptionally active meteor showers ($\sim$10,000 meteors per hour; Jenniskens 1995). The outburst activity is strongly associated with years when the Earth and 21P closely approach each other, suggesting that the comet is presently ejecting meteoroids.

Thermal radiation from large grains in a comet trail is easily detected at IR wavelengths from space-based telescopes (Reach et al. 2007; Sykes & Walker 1992), where the emission from warm ($\simeq$100 K) dust peaks. We examined our MIPS 24 μm image of 21P (obtained at 2.4 AU) for dust trail emission along the projected velocity vector of the comet (Figure 8). No trail is detected with a 3σ surface brightness upper limit of 0.3 MJy sr^{-1} $pixel^{-1}$. Assuming a typical trail grain temperature of $\approx 300\, r_h^{-0.5} = 193$ K (Sykes & Walker 1992), the latter surface brightness corresponds to an IR optical depth of 2.2×10^{-9}. Our upper limit is larger than the typical comet trail observed in other *Spitzer* MIPS images (Reach et al. 2007); thus it is possible that 21P still has a dust trail. Miura et al. (2007), using deep R-band imaging of 21P, do not detect the presence of brightness enhancements at the expected position of the dust trail, and derive an upper limit to the number density of trail grains to be 10^{-10} m^{-3}. Using similar assumptions (typical grain size of 1 mm), and assuming a typical trail thickness of $\sim 10^4$ km (Reach et al. 2007), our MIPS optical depth limit suggests a number density $\lesssim 7 \times 10^{-11}$ m^{-3} —slightly lower than the optically determined value. Miura et al. (2007) also estimate the dust trail number density from meteor shower activities. Their lower limit (8×10^{-15} m^{-3}) is about four orders of magnitude smaller than our upper limit. For comparison, the trail grain number density for 81P/Wild is $\sim 10^{-9}$ m^{-3} (Ishiguro et al. 2003), and for 67P/Churyumov-Gerasimenko is $\sim 10^{-11}$ m^{-3} (Kelley et al. 2008). Altogether, the evidence suggests comet 21P has a dust trail fainter than the detectable limits of the available observations.

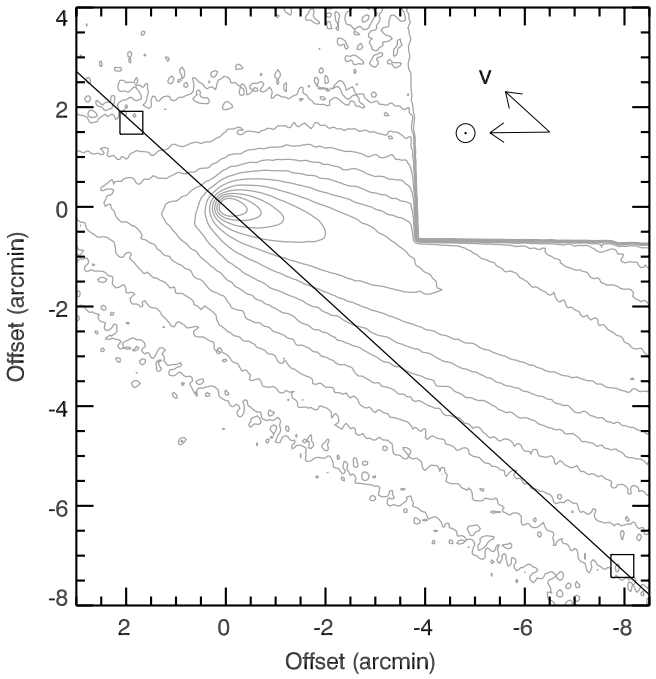

Figure 8. A smoothed version of the *Spitzer* MIPS 24 μm image (contours) and the projected orbit of the comet 21P/Giacobini-Zinner (solid black line). The image has been smoothed with a Gaussian function, 6.4″ FWHM. The contours are logarithmically spaced, with each step being a 50% increase in surface brightness, starting at 0.3 MJy sr^{-1}, and ending at 25.9 MJy sr^{-1}. The boxes mark the areas where we estimated the trail upper limit from the standard deviation of an 11 × 11 pixel aperture.

4. CONCLUSIONS

We have presented new optical and *Spitzer* IR observations of comet 21P/Giacobini-Zinner obtained during its 2005 apparition. Analysis of the optical imagery indicates that 21P was dusty (peak $Af\rho = 131$ cm^{-1}) and active out to heliocentric distances $\gtrsim$3.3 AU following a logarithmic slope with r_h of -2.04. The onset of nucleus activity occurred at a pre-perihelion distance $r_h \simeq 3.80$ AU (-375 days pre-perihelion), similar in behavior to that observed in the 1991 apparition. The derived average coma colors, $V - R = 0.524 \pm 0.003$, $R - I = 0.487 \pm 0.004$

are slightly redder than solar, comparable to colors derived for other Jupiter-family comets. Pre-perihelion observations during quiescence yields a nucleus radius of 1.82 ± 0.05 km.

Spitzer IRAC images obtained at $r_h = 2.4$ AU post-perihelion exhibit an extensive coma with a prominent dust tail, where excess emission (over the dust continuum) in the 4.5 μm image at cometocentric distances of $\sim 10^4$ km likely arises from CO_2, although a distributed source of CO cannot be discounted. The upper limits to the production rates are $Q_{CO_2} \leqslant (5.13 \pm 0.75) \times 10^{25}$ molecules s^{-1} and $Q_{CO} \leqslant (6.01 \pm 0.89) \times 10^{26}$ molecules s^{-1}. The surface brightness of the gas emission is observed to peak along the sun angle, while the dust tail peaks near the anti-sunward angle. A search for dust trail emission along the projected velocity vector of comet 21P using our MIPS 24 μm image ($r_h = 2.4$ AU), yielded no trail (3σ surface brightness upper limit of 0.3 MJy sr^{-1} $pixel^{-1}$), suggesting that the number density of trail particles (typical particle size $\sim$ 1 mm) is $\lesssim 7 \times 10^{-11}$ m^{-3}. The bolometric albedo of 21P derived from the contemporaneous optical and *Spitzer* observations is $A(\theta = 22^\circ) = 0.11$, slightly lower than the values derived for other comets at the same phase angle.

This work is based on observations made with the *Spitzer* Space Telescope, which is operated by the Jet Propulsion Laboratory, California Institute of Technology under a contract with NASA. Support for this work was provided by NASA through an award issued by JPL/Caltech. Support for this work was also provided by NASA through contracts 123741, 127835, and 1256406 issued by JPL/Caltech to the University of Minnesota. C.E.W. acknowledges support from the National Science Foundation grant AST-0706980. M.S.K. acknowledges support from the University of Minnesota Doctoral Dissertation Fellowship. J.P. was supported, in part, by the NASA Planetary Astronomy Program, and by NASA through contract 1278383 issued by JPL/Caltech to the University of Hawaii and the Scientific Grant Agency VEGA of the Slovak Academy of Sciences, 2/4002/04. The authors wish to thank Dr. Karen Meech for her insightful discussions, as well as an anonymous referee whose comments and suggestions improved the clarity of this manuscript.

Facilities: Spitzer (IRAC, MIPS) UH 2.2m (Tek2048 CCD)

REFERENCES

Allen, C. W. 1973, Astrophysical Quantities (3rd ed; London: Athlone Press)
A'Hearn, M. F., Schleicher, D. G., Feldman, P. D., Millis, R. L., & Thompson, D. T. 1984, AJ, 89, 579
A'Hearn, M. F., et al. 1995, Icarus, 118, 223
A'Hearn, M. F., et al. 2005, Science, 310, 258
Becklin, E. E., Farihi, J., Jura, M., Song, I., Weinberger, A. J., & Zuckerman, B. 2005, ApJ, 632, L119
Beech, M. 1986, AJ, 91, 159
Belton, M. J. S., et al. 2007, Icarus, 191, 573
Bockelée-Morvan, D., Crovisier, J., & Gerard, E. 1990, A&A, 238, 382
Bockelée-Morvan, D., et al. 2002, Earth Moon Planets, 89, 531
Capria, M. T. 2002, Earth Moon Planets, 89, 161
Crovisier, J. 1999, Nature, 399, 640
Crovisier, J., & Encrenaz, T. 1983, A&A, 126, 170
Crovisier, J., et al. 1999a, in The Universe as Seen by ISO, ed. P. Cox, & M. F. Kessler (Noordwijk: ESA), 137
Crovisier, J., et al. 1999b, in The Universe as Seen by ISO, ed. P. Cox, & M. F. Kessler (Noordwijk: ESA), 161
Davidsson, B., & Skorov, Y. 2002, Icarus, 156, 223
Dello Russo, N., Vervack, R. J., Weaver, H. A., Biver, N., Bockelée-Morvan, D., Crovisier, J., & Lisse, C. M. 2007, Nature, 448, 172
Farnham, T. L., et al. 2007, Icarus, 191, 146
Fazio, G. G., et al. 2004, ApJS, 154, 10
Feaga, L. M., A'Hearn, M. F., Sunshine, J. M., Groussin, O., & Farnham, T. L. 2007, Icarus, 190, 345
Fernández, Y., Jewitt, D. C., & Sheppard, S. S. 2001, ApJ, 553, L197
Fernie, J. D. 1983, PASP, 95, 782
Ferrín, I. 2005, Icarus, 178, 493
Fink, U., & Hicks, M. D. 1996, ApJ, 459, 729
Gehrz, R. D., & Ney, E. P. 1992, Icarus, 100, 162
Gunnarsson, M. 2003, A&A, 398, 353
Gunnarsson, M., et al. 2003, A&A, 402, 383
Harker, D. E., Woodward, C. E., Wooden, D. H., Trujillio, C., & Fisher, S. 2007, Icarus, 190, 432
Huebner, W. F., Keady, J. J., & Lyon, S. P. 1992, Ap&SS, 195, 1
Ishiguro, M., Kwon, S. M., Sarugaku, Y., Hasegawa, S., Usui, F., Nishiura, S., Nakada, Y., & Yano, H. 2003, ApJ, 589, L101
Ishiguro, M., Sarugaku, Y., Ueno, M., Miura, N., Usui, F., Chun, M.-Y., & Kwon, S. M. 2007, Icarus, 189, 169
Jenniskens, P. 1995, A&A, 295, 206
Jewitt, D. C. 2002, AJ, 123, 1039
Jewitt, D. C., & Danielson, G. E. 1984, Icarus, 60, 435
Jewitt, D. C., & Meech, K. J. 1986, ApJ, 310, 937
Kadono, T., et al. 2007, ApJ, 661, L89
Kelley, M. S., Reach, W. T., & Lien, D. J. 2008, Icarus, 193, 572
Kelley, M. S., et al. 2006, ApJ, 651, 1256
Kolokolova, L., Hanner, M. S., Levasseur-Regourd, A.-C., & Gustafson, B. Å. S. 2005, in Comets II, ed. M. Festou, H. U. Keller, & H. A. Weaver (Tucson, AZ: Univ. of Arizona Press)
Lamy, P., Toth, I., Fernández, Y., & Weaver, H. 2005, in Comets II, ed. M. Festou, H. U. Keller, & H. A. Weaver (Tucson, AZ: Univ. of Arizona Press)
Landolt, A. U. 1992, AJ, 104, 340
Landsman, W. B. 1993, Astron. Data Anal. Software Syst. II, 52, 246
Leibowitz, E. M., & Brosch, N. 1986, Icarus, 68, 430
Lunine, J. L., & Gautier, D. 2004, in Comets II, ed. M. Festou, H. U. Keller, & H. A. Weaver (Tucson, AZ: Univ. of Arizona Press)
Makovoz, D., & Khan, I. 2005, in ASP Conf. Ser. 347, Astronomical Data Aanalysis Software and Systems XIV, ed. P. Shopbell, M. Britton, & R. Ebert (San Francisco, CA: ASP)
Meech, K., & Svoreň, J. 2004, in Comets II, ed. M. Festou, H. U. Keller, & H. A. Weaver (Tucson, AZ: Univ. of Arizona Press)
Miura, N., Ishiguro, M., Sarugaku, Y., Usui, F., & Ueno, M. 2007, Dust Planetary Syst., 643, 23
Mueller, B. E. A. 1992, Proc. Asteriods, Comets, Meteors (Houston, TX: LPI)
Mumma, M. J., DiSanti, M. A., Dello Russo, N., Magee-Sauer, K., & Rettig, T. W. 2000, ApJ, 531, L155
Press, W. H., Teukolsky, S. A., Vetterling, W. T., & Flannery, B. P. 1992, Numerical Recipes: the Art of Scientific Computing (2nd ed; Cambridge: Cambridge Univ. Press)
Prialnik, D. 2002, Earth Moon Planets, 89, 27
Prialnik, D., et al. 2004, in Comets II, ed. M. Festou, H. U. Keller, & H. A. Weaver (Tucson, AZ: Univ. of Arizona Press)
Reach, W. T., Kelley, M. S., & Sykes, M. V. 2007, Icarus, 191, 298
Reach, W. T., et al. 2005, ApJ, 635, L161
Rieke, G. H., et al. 2004, ApJS, 154, 25
Russel, H. 1916, ApJ, 43, 173
Snodgrass, C., Fitzsimmons, A., & Lowry, S. C. 2005, A&A, 444, 287
Spitzer Science Center 2006, in Infrared Array Camera Data Handbook (Pasadena, CA: SSC), http://ssc.spitzer.caltech.edu/irac/dh/
Su, K. Y. L., et al. 2007, ApJ, 657, L41
Sykes, M. V., Lebofsky, L. A., Hunten, D. M., & Low, F. 1988, Science, 232, 1115
Sykes, M. V., & Walker, R. G. 1992, Icarus, 95, 180
Tancredi, G., Fernández, J. A., Rickman, H., & Licandro, J. 2000, A&AS, 146, 73
von Rosenvinge, T. T., Brandt, J. C., & Farquhar, R. W. 1986, Science, 232, 353
Weaver, H. A., et al. 1999, Icarus, 142, 482
Werner, M. W., et al. 2004, ApJS, 154, 1
Wooden, D. H., Charnley, S. B., & Ehrenfreund, P. 2004, in Comets II, ed. M. Festou, H. U. Keller, & H. A. Weaver (Tucson, AZ: Univ. of Arizona Press)
Woodward, C. E., Kelley, M. S., Bockelée-Morvan, D., & Gehrz, R. D. 2007, ApJ, 671, 1065